

PSD-95 family MAGUKs are essential for anchoring AMPA and NMDA receptor complexes at the postsynaptic density

Xiaobing Chen^a, Jonathan M. Levy^b, Austin Hou^a, Christine Winters^a, Rita Azzam^a, Alioscka A. Sousa^c, Richard D. Leapman^c, Roger A. Nicoll^b, and Thomas S. Reese^{a,1}

^aLaboratory of Neurobiology, National Institute of Neurological Disorders and Stroke, National Institutes of Health, Bethesda, MD 20892; ^bDepartment of Cellular and Molecular Pharmacology, University of California, San Francisco, CA 94158; and ^cLaboratory of Cellular Imaging and Macromolecular Biophysics, National Institutes of Biomedical Imaging and Bioengineering, National Institutes of Health, Bethesda, MD 20892

Contributed by Thomas S. Reese, October 28, 2015 (sent for review October 16, 2015; reviewed by Robert C. Malenka and Richard J. Weinberg)

The postsynaptic density (PSD)-95 family of membrane-associated guanylate kinases (MAGUKs) are major scaffolding proteins at the PSD in glutamatergic excitatory synapses, where they maintain and modulate synaptic strength. How MAGUKs underlie synaptic strength at the molecular level is still not well understood. Here, we explore the structural and functional roles of MAGUKs at hippocampal excitatory synapses by simultaneous knocking down PSD-95, PSD-93, and synapse-associated protein (SAP)102 and combining electrophysiology and transmission electron microscopic (TEM) tomography imaging to analyze the resulting changes. Acute MAGUK knockdown greatly reduces synaptic transmission mediated by α -amino-3-hydroxyl-5-methyl-4-isoxazole-propionate receptors (AMPA) and *N*-methyl-D-aspartate receptors (NMDARs). This knockdown leads to a significant rise in the number of silent synapses, diminishes the size of PSDs without changes in pre- or postsynaptic membrane, and depletes the number of membrane-associated PSD-95-like vertical filaments and transmembrane structures, identified as AMPARs and NMDARs by EM tomography. The differential distribution of these receptor-like structures and dependence of their abundance on PSD size matches that of AMPARs and NMDARs in the hippocampal synapses. The loss of these structures following MAGUK knockdown tracks the reduction in postsynaptic AMPAR and NMDAR transmission, confirming the structural identities of these two types of receptors. These results demonstrate that MAGUKs are required for anchoring both types of glutamate receptors at the PSD and are consistent with a structural model where MAGUKs, corresponding to membrane-associated vertical filaments, are the essential structural proteins that anchor and organize both types of glutamate receptors and govern the overall molecular organization of the PSD.

MAGUKs | knockdown | EM tomography | NMDAR | AMPAR

The postsynaptic density (PSD) at excitatory glutamatergic synapses, appearing in electron micrographs as a prominent electron-dense thickening lining the postsynaptic membrane (1) is a complex macromolecular machine positioned across from synaptic vesicle release sites at the presynaptic active zone. The PSD clusters and organizes neurotransmitter receptors and signaling molecules at the postsynaptic membrane, transmits and processes synaptic signals, and can undergo structural changes to encode and store information (2–5). Two types of ionotropic glutamate receptors, AMPA receptors (AMPA) and NMDA receptors (NMDARs), present at PSDs of excitatory synapses (6–10) mediate almost all synaptic transmission in the brain (11). Biochemistry and mass spectrometry of the detergent-extracted cellular fraction of PSDs have additionally identified many proteins associated with AMPAR and NMDAR complexes (12, 13).

The membrane-associated guanylate kinases (MAGUKs), a class of abundant scaffold proteins consisting of PSD-95, PSD-93, synapse-associated protein (SAP)102, and SAP97, interact directly with NMDARs (14–18). These MAGUK proteins share conserved

modular structures consisting of three PDZ domains (19, 20) and one SH3-GK supermodule (21). PDZ domains of MAGUKs bind to a conserved motif at the extreme C-terminal region of GluN2 subunits of NMDARs (16, 22). PSD-95 controls the number of AMPARs at the PSD through interactions with auxiliary proteins, such as Stargazin/TARPs in complex with AMPARs (23–25). Single-particle tracking of AMPARs provides evidence that AMPAR/Stargazin complexes are stabilized by PSD-95 at the membrane (26), where PSD-95 is thought to provide hot spots for accumulating AMPARs at synapses (27, 28). Germ-line knockout of PSD-95 reduces AMPAR transmission with little effects on NMDARs (29), whereas acute loss of single members of the MAGUK family decreases primarily AMPAR-mediated synaptic transmission (30–32), and removal of multiple MAGUKs results in greater losses of transmission mediated by both AMPARs and NMDARs (30).

PSD-95 and PSD-93 include N-terminal palmitoylation sites that enable PSD-95 and PSD-93 to associate with membrane lipids. N-terminal palmitoylation of PSD-95 is necessary for its synaptic localization, clustering of receptors (33–35), and stability at the PSD (36). PSD-95 palmitoylation regulates synaptic strength by controlling the accumulation of AMPARs at the PSD (35). Consistent with these results, a recent immunogold electron microscopy (immuno-EM) mapping of the positions of the two ends of the PSD-95 molecule at the PSD shows that its N terminus is located at the membrane, whereas its C terminus is farther

Significance

The postsynaptic density (PSD) at the glutamatergic excitatory synapse is a macromolecular machine that underlies synaptic transmission and information storage. Membrane-associated guanylate kinases (MAGUKs), the major scaffolding proteins at the PSD, are positively correlated with synaptic maturation and strength, but how MAGUKs sustain the strength of synaptic transmission remains unclear. Here, we remove three MAGUK proteins from neurons and find significant reductions in synaptic transmission by AMPARs and NMDARs with a concomitant reduction in PSD sizes and core scaffold and transmembrane structures. Our results show how MAGUKs anchor and organize both types of glutamate receptors, thereby regulating the strength of excitatory synapses.

Author contributions: X.C., J.M.L., R.D.L., R.A.N., and T.S.R. designed research; X.C., J.M.L., A.H., C.W., R.A., and A.A.S. performed research; J.M.L. contributed new reagents/analytic tools; X.C., J.M.L., and A.H. analyzed data; and X.C., J.M.L., R.D.L., R.A.N., and T.S.R. wrote the paper.

Reviewers: R.C.M., Stanford University School of Medicine; and R.J.W., University of North Carolina at Chapel Hill.

The authors declare no conflict of interest.

Freely available online through the PNAS open access option.

¹To whom correspondence should be addressed. Email: treese@ninds.nih.gov.

This article contains supporting information online at www.pnas.org/lookup/suppl/doi:10.1073/pnas.1517045112/-DCSupplemental.

away from the membrane in a relatively extended configuration, where it is vertically oriented with respect to the membrane (3, 4, 37). In contrast, neither SAP102 nor SAP97 has palmitoylation sites. SAP97 contains a L27 domain at the N terminus (31, 38), which might be involved in self-association, and has a role in sorting and trafficking of AMPARs and NMDARs (39) but is not required for basal synaptic transmission (40).

The MAGUK family proteins interact with a host of other proteins in the PSD, such as GKAP (41, 42), which binds to the GK domain of the MAGUKs, whereas GKAPs in turn bind Shank and Homer (43–45). Both Shank and Homer can interact with actin-associated proteins, thus indirectly linking the core PSD structure to the actin system prevalent in the cytoplasm of dendritic spines (45). MAGUKs interact with signaling complexes such as AKAPs (46, 47), K channels (48), and postsynaptic adhesion molecules such as neuroligin (49, 50). With an average density of 300–400 molecules per PSD (51, 52), the MAGUKs outnumber glutamate receptors by a significant margin. With so many potential binding partners, the MAGUKs are positioned to play an important role in organizing glutamate receptors as well as other scaffolding and signaling molecules at the PSD (53).

We have examined the consequences of knocking down three key MAGUKs on excitatory synaptic transmission and found an ~80% reduction in both AMPAR and NMDAR synaptic responses (54). Interestingly, despite the rather ubiquitous distribution of MAGUKs at excitatory synapses, the reduction in synaptic AMPAR-mediated transmission appeared to be attributable primarily to an all-or-none loss of functional synapses. We present evidence that after the knockdown, there is an initial uniform decrease in AMPARs across all synapses, but over a 4-d period, a consolidation process in which a “winner-take-all” phenomenon occurs (54).

Here, we have used EM tomography (3, 4) to study the structural effects of knocking down the three key MAGUKs at the PSD to develop a molecular model of the organization of the core PSD structure in intact hippocampal spine synapses. PSDs in intact synapses show numerous regularly spaced and membrane-associated vertical filaments containing PSD-95 in extended conformation connecting with NMDAR and AMPAR-type complexes. These vertical structures in turn contact horizontal elements, resulting in a molecular scaffold supporting a core PSD structure (3, 4, 37). Thus, vertical filaments appear to be of crucial importance in sustaining the core PSD structure. Here, we show that knocking down three key synaptic MAGUKs results in a profound loss of vertical filaments and the electron-dense materials manifested by the PSD. The loss of MAGUKs is accompanied by a dramatic loss of both NMDAR- and AMPAR-type structures at the PSD.

Results

MAGUKs Are Required for Normal Synaptic AMPAR and NMDAR Transmission. We developed a chained-miRNA construct to knock down PSD-95, PSD-93, and SAP102 to investigate the changes in the molecular organization and synaptic function resulting from acute knockdown of a family of MAGUKs. Use of an RNAi-mediated knockdown construct results in acute loss of MAGUK protein and does not trigger the compensatory mechanisms that obscure the effects of germ-line MAGUK knockout (30). The construct consists of the CAG hybrid promoter driving EGFP, followed by miRNA sequences targeting PSD-93, PSD-95, and SAP102 placed sequentially in the EGFP 3' UTR (Fig. 1A). Expression of a single construct targeting the three synaptic MAGUKs allows for simple transfection of neurons and reliable confirmation of transfection by GFP fluorescence (Fig. 1B). SAP97, which has no known role in basal synaptic transmission (40), was not targeted. The miRNA construct was packaged in lentivirus to optimize infection efficiency, which appeared to be very high in cultured hippocampal neurons because essentially all

neurons were fluorescent when overlaid with transmission light microscopy images at low magnification (Fig. 1B).

Expression of the MAGUK miRNA construct substantially reduced the levels of PSD-93, PSD-95, and SAP102 in dissociated hippocampal neurons. Western blot analyses comparing cell lysates of neuronal cultures treated either with lentivirus-GFP control (Lenti-GFP) or lentivirus triple-MAGUK knockdown (Lenti-KD) showed a marked reduction of PSD-95, PSD-93, and SAP102 levels following knockdown (Fig. 1C). RT-PCR showed that mRNA levels of PSD-95, PSD-93, and SAP102 were diminished to 11–16% of control transcript (Fig. S1), demonstrating the effectiveness of the knockdown construct. The discrepancy between the mRNA level and protein level is likely to reflect rate-limiting turnover of the MAGUK proteins, especially when these proteins form molecular complexes and are localized to cellular compartments in neurons.

Glutamatergic excitatory postsynaptic currents (EPSCs) evoked by local stimulation of presynaptic processes (55) allowed measurements of the effect of MAGUK knockdown. Whole-cell recordings simultaneously measured EPSCs from a transfected miRNA-expressing neuron and a neighboring untransfected neuron (Fig. 1D1 and D2). Lipofectamine was used to sparsely transfect the dissociated cultures. The amplitudes of AMPAR EPSCs (Fig. 1E1 and E2) and NMDAR EPSCs (Fig. 1F1 and F2) were reduced ~73% and ~61%, respectively, after transfection with MAGUK miRNA, as normalized to simultaneously recorded control neurons. These reductions are quantitatively similar to those following viral transduction of the MAGUK miRNA in virally transduced hippocampal organotypic slice cultures (54). Furthermore, miniature EPSCs (mEPSCs) were examined to define the basis of the reduction in AMPAR transmission. Knockdown of the MAGUKs caused a relatively small (~16%) reduction in mEPSC amplitude (Fig. 1G and H), suggesting some loss of AMPARs at each synapse. A much larger reduction (~81%) in mEPSC frequency (Fig. 1I and J) indicates the silencing of some synapses. The reduction in mEPSC amplitude, however, will cause a subset of events to fall below the detection threshold because of electrical noise and therefore may underrepresent the true decrease in quantal size. To determine how this threshold influences the mEPSC recordings, we performed a series of control experiments recording Sr²⁺-evoked asynchronous EPSCs (aEPSCs). These aEPSCs are quantal events that occur only at the subset of synapses undergoing evoked release and can therefore be directly compared with the remaining synchronous component of the evoked EPSC. aEPSCs are identical in amplitude to mEPSCs, can be temporally isolated, and are amenable to analysis of quantal size and aEPSC frequency (56–58). To observe the error that the mEPSC noise threshold introduced, we compared the reduction in aEPSCs to the reduction in the remaining synchronous component of the evoked EPSC when the holding potential was changed from –70 to –20 mV, causing a large pure decrease in quantal size. Following this change in membrane potential, the synchronous component of the AMPAR response would be predicted to decrease by 5/7, to 28.5%, because of the reduction in the driving force. We confirmed this, because a paired comparison of neurons, recorded at –70 mV, followed by –20 mV, finds on average, 29.7% of EPSC remaining after the change in membrane potential (Fig. S2A). Importantly, the reduction in EPSCs results from a uniform reduction in the postsynaptic response to neurotransmitter release and therefore corresponds to a pure decrease in quantal size. If the detection threshold were playing no role, we would expect to find an equivalent reduction in aEPSC amplitude, with no reduction in aEPSC frequency. Rather than a pure decrease in aEPSC amplitude, we find equal reductions of around 50% in both aEPSC frequency and amplitude (Fig. S2B and C). These results suggest that a portion of the reduction in mEPSC frequency (Fig. 1J) is secondary to the reduction in mEPSC amplitude because of a subset of events falling below the detection threshold, and the actual reduction in aEPSC amplitude is more substantial than the reduction actually observed (Fig. 1H). Thus,

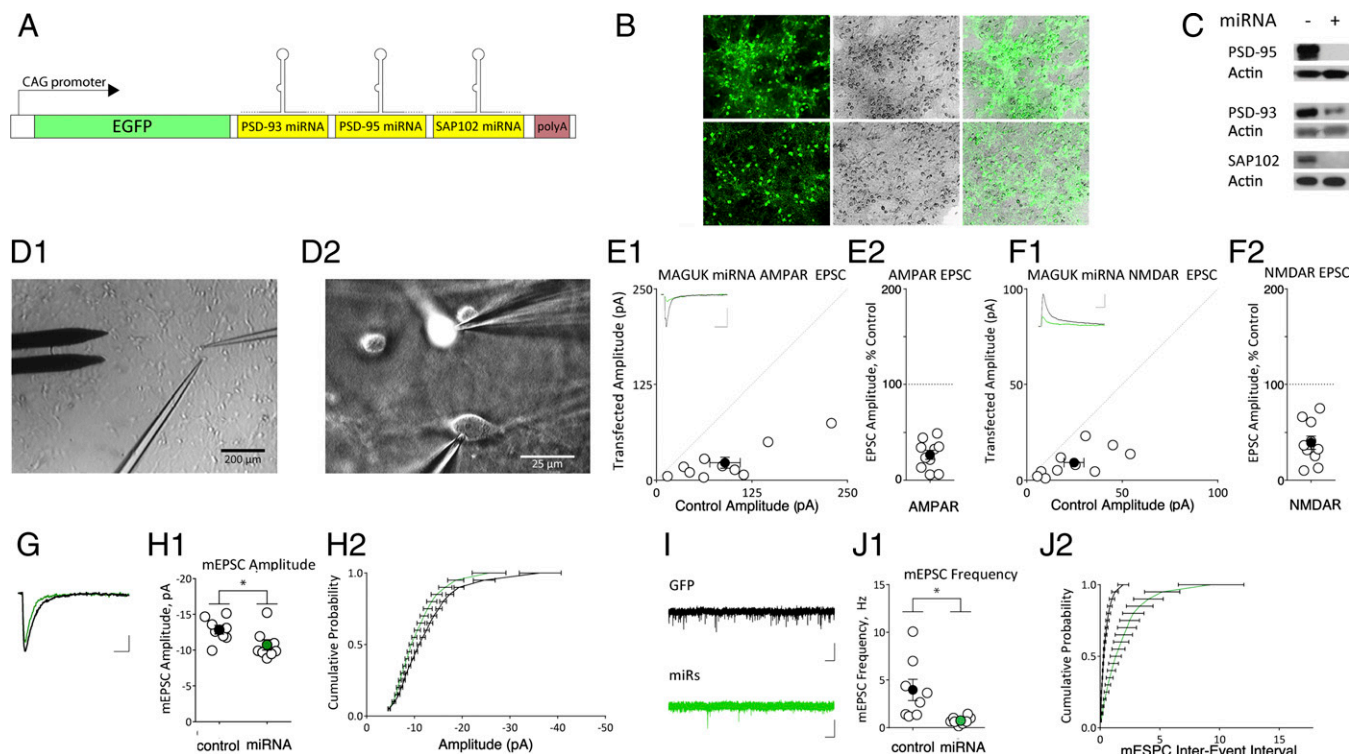


Fig. 1. Triple knockdown of PSD MAGUKs. (A) CAG hybrid promoter drives EGFP with a synthetic 3' UTR containing miRNA sequences targeting PSD-93, PSD-95, and SAP102. (B) Efficient transduction of miRNA by lentivirus in dissociated hippocampal neurons. (B, Upper) Confocal image of hippocampal cultures infected with control Lenti-GFP (Left), DIC image of the same field showing the prominent cell bodies of neurons appearing as dark dots (Center), and overlay showing that essentially all cell bodies in field are infected (Right). (B, Lower) Hippocampal cultures infected with lentivirus miRNA that knocks down PSD-95, PSD-93 and SAP102 (triple-MAGUK knockdown) (Left), DIC image of the same field showing the cell bodies of neurons (Center), and overlay showing that essentially all cells are infected (Right). (C) Infection of dissociated hippocampal neurons with lentivirus expressing the MAGUK miRNA construct substantially reduces the amount of PSD-95, PSD-93, and SAP102 protein. (D1) Simultaneous recording setup with two recording electrodes and stimulation electrode. (D2) High-resolution depiction of recording setup showing simultaneous recording of a transfected fluorescent neuron and a neighboring control neuron. (E1 and E2) Scatter plots showing reductions in AMPAR EPSCs in MAGUK miRNA-transfected neurons compared with untransfected controls. The scatter plots of EPSCs show single pairs (open circles) and mean \pm SEM (filled circle) (AMPA, $26.6 \pm 4.8\%$ control, $P < 0.01$, $n = 10$). (F1 and F2) Scatter plots showing reductions in NMDAR EPSCs in MAGUK miRNA-transfected neurons compared with untransfected controls (NMDAR, $39.3 \pm 7.0\%$ control, $P < 0.01$, $n = 10$). The scatter plots of EPSCs show single pairs (open circles) and mean \pm SEM (filled circle). (G) Representative average mEPSC traces showing control (black) and experimental (green) mEPSCs. (H1) mEPSC amplitude in neurons expressing MAGUK miRNA. The plot shows single pairs (open circles) and means \pm SEM (filled circles). mEPSC amplitude is significantly reduced in neurons expressing MAGUK miRNA (control, -12.86 ± 0.58 pA; miRNA, -10.75 ± 0.72 pA, $n = 8$, $P < 0.05$). (H2) The cumulative distribution of mEPSC amplitude. Control is shown in black, and experimental is in green. The cumulative distribution functions show no irregularities. (I) Representative sample traces of mEPSC frequency recorded in the presence of $0.5 \mu\text{M}$ TTX. (J1 and J2) mEPSC frequency plot showing single pairs (open circles) and means \pm SEM (filled circles). mEPSC frequency is significantly reduced in neurons expressing MAGUK miRNA (control, 3.96 ± 1.12 Hz; miRNA, 0.75 ± 0.14 Hz, $n = 8$, $P < 0.05$). The cumulative distribution plot shows no irregularities.

many synapses are likely functionally silenced following MAGUK knockdown, and the remaining synapses are weakened.

Triple-MAGUK Knockdown Reduces Length of the PSD. Conventional thin-section (~ 80 -nm-thick) EM was used to determine the effects of triple-MAGUK knockdown (Fig. 2 A–D). A fluorescent EGFP tag in the miRNA made it possible to identify cell bodies and dendritic processes of infected neurons by immuno EM (Fig. 2B). Immunogold labeling using an antibody to the GFP-marked infected neurons permitted unambiguous evaluation of the morphological effects on PSDs of triple-MAGUK knockdown (Fig. 2B). There was a significant reduction in the mean total lengths of PSDs measured along the postsynaptic membrane after the knockdown (Fig. 2E). Because knockdown turned out to affect virtually all neurons (Fig. 1B), we reasoned that the knockdown effects on the length of PSDs might be measurable directly from randomly sampled dendritic spines that were fixed directly following the knockdown (Fig. 2C and D). Indeed, the distribution of PSD length derived from the direct measurements was identical to that of PSDs from spines identified by immunogold labeling, so the two datasets were pooled (Fig. 2E). The average combined length of PSDs were as follows: 331 ± 93 nm

for the control (no virus) (mean \pm SD; $n = 143$; Fig. 2F); 304 ± 112 nm for the Lenti-GFP control [$n = 208$, $P = 0.05$; one-way ANOVA, not significant (NS); significance level, $P = 0.01$]; and 158 ± 103 nm for the Lenti-KD ($n = 252$, $P < 0.001$; ANOVA, tested against both controls; Fig. 2F and G). Distribution of the PSD length for the controls showed an expected Gaussian-shaped peak centered around 320 nm, close to the typical PSD diameter of 360 nm (59), whereas the knockdown group showed two peaks centered at ~ 150 and 17 nm, where very little electron-dense PSD material was evident. The latter group accounted for 17.5% of total synapse population.

These data show that with MAGUK knockdown, a subpopulation of close to 20% of synapses loses essentially all of the electron-dense structure at their PSDs (Fig. 2E). Furthermore, the reduction in PSD length is not uniform across all synapses because a scaled-down length distribution in the controls does not fit with the length distribution after knockdown. It is also instructive to compare the combined PSD length following a partial PSD-95 knockdown (37) with the triple-MAGUK knockdown. Although the mean combined PSD length is unchanged after a partial PSD-95 knockdown (37), it is reduced by $\sim 50\%$ following the

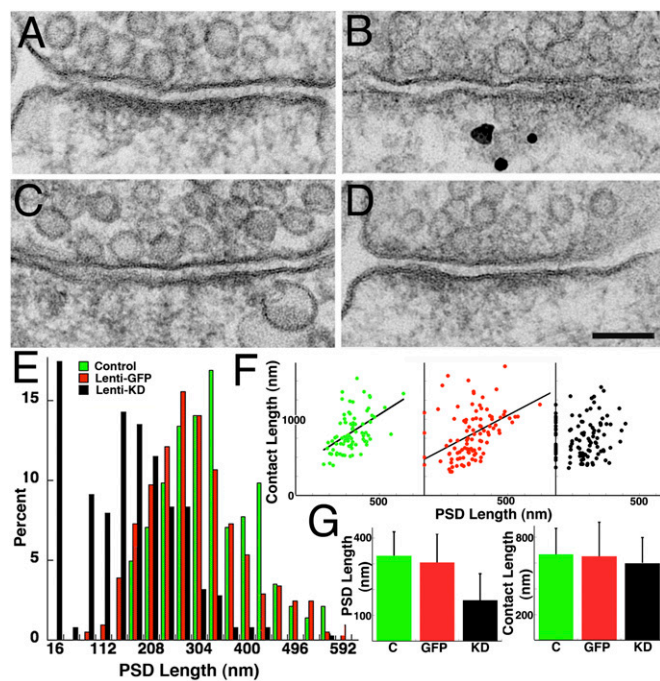


Fig. 2. Triple-MAGUK knockdown reduces PSD length. (A) Electron micrograph of a spine synapse from a control showing typical continuous electron-dense PSDs. In the knockdown group, 62% synapses with electron-dense PSDs fall into a Gaussian distribution peaking at a PSD diameter of 352 nm, whereas 24% of synapses do not show apparent electron-dense PSDs. The fact that this population of synapses, present in low abundance in controls, increased significantly after knockdown suggests that they represent immature excitatory synapses. These data are in general agreement with the 2D analysis showing that about 20% of synapses completely lose their PSDs, leaving an ~70% reduction in area of the PSDs in the remaining synapses. Further examination of the PSD size distribution in the knockdown group showed that there is still a significant population of synapses that possess sizable electron-dense PSDs; for example, 38% of synapses manifested PSD diameters larger than or equal to 225 nm, whereas 52% of synapses with PSDs had diameters larger than or equal to 175 nm (Fig. 3D), and 17% of synapses had a PSD diameter larger than or equal to 315 nm. Whether these remaining large PSDs are attributable to incomplete knockdown, incomplete structural turnover, or some unknown compensatory processes at synapses remains unclear.

triple-MAGUK knockdown, suggesting that triple-MAGUK knockdown significantly reduces the overall size of PSDs.

Minimal Structural Changes in Pre- and Postsynaptic Membranes Accompany Knockdown.

At synapses shown by immuno-EM to be affected by knockdown, the structure of the corresponding presynaptic terminals appeared normal, and synaptic vesicles lined up along the presynaptic membrane, even at places where the corresponding electron-dense PSD was absent (Fig. 2A–D). To quantitatively assess whether the reduction in PSD length in 2D electron micrographs might be associated with structural changes at either pre- or postsynaptic terminals, we measured the contact lengths of synapses—defined as the length of the postsynaptic membrane in register with the presynaptic terminal—from the set of synapses used to measure PSD lengths. The contact length remained unchanged (Fig. 2G): 665 ± 203 nm for control without virus ($n = 77$); 651 ± 265 nm for Lenti-GFP control ($n = 101$, $P = 1$); and 598 ± 198 nm for Lenti-KD ($n = 114$, $P = 0.14$). This result indicated that even with evident loss of the electron-dense structures at the PSD, the pre- and the postsynaptic membranes remain normal.

Contact length, as expected, correlates linearly and positively with PSD length in controls [no virus control: $r = 0.49$ (critical value, $r = 0.22$), $n = 77$, $P < 0.001$, two tails; Lenti-GFP control: $r = 0.48$ (critical value, $r = 0.19$), $n = 101$, $P < 0.001$; Fig. 2], indicating that the contact length is positively correlated with both PSD size and spine size (60, 61) in control synapses. However, the correlation is lost in Lenti-KD synapses [$r = 0.15$ (critical value, $r = 0.18$), $n = 113$, $0.1 < P < 0.2$; Fig. 2F]. The lack of correlation between PSD length and contact length, and thus

likely spine size, following knockdown (Fig. 2F) suggests that larger spines lose significantly more of their electron-dense PSD material than smaller spines.

Triple-MAGUK Knockdown Reduces PSD Area. Conventional thin-section EM of synapses provided images for measuring 2D parameters, such as PSD length and synapse contact length. However, sampling is confined to one plane within an ~100-nm-thick section, which is less than the average diameter of a PSD (360 nm). Thus, on average, only one-third or less of the PSD is sampled, which might lead to biases in the 2D EM data. These limitations can be overcome by making 3D reconstructions of sections 1- to 2- μ m-thick with scanning transmission EM (STEM) tomography, which avoids the chromatic aberration that blurs images in thick sections (62, 63). The thicker sections contain entire PSDs, allowing the PSDs to be completely reconstructed without serial sectioning (Fig. 3A–C). Analyses from STEM tomograms revealed that the areas of electron-dense thickening typical of PSDs decreased significantly following the knockdown (Fig. 3B), from $0.104 \pm 0.056 \mu\text{m}^2$ ($n = 70$, control) to $0.032 \pm 0.042 \mu\text{m}^2$ ($n = 172$, Lenti-KD; $P < 0.0001$), and the corresponding PSD diameters were 352 ± 95 nm ($n = 53$ excluding the empty spines, control) and 237 ± 94 nm ($n = 107$, Lenti-KD). Distributions of PSD diameter (Fig. 3D) show bimodal distributions in both control and knockdown groups. In the control group, 76% of synapses with electron-dense PSDs fall into a Gaussian distribution peaking at a PSD diameter of 352 nm, whereas 24% of synapses do not show apparent electron-dense PSDs. The fact that this population of synapses, present in low abundance in controls, increased significantly after knockdown suggests that they represent immature excitatory synapses. These data are in general agreement with the 2D analysis showing that about 20% of synapses completely lose their PSDs, leaving an ~70% reduction in area of the PSDs in the remaining synapses. Further examination of the PSD size distribution in the knockdown group showed that there is still a significant population of synapses that possess sizable electron-dense PSDs; for example, 38% of synapses manifested PSD diameters larger than or equal to 225 nm, whereas 52% of synapses with PSDs had diameters larger than or equal to 175 nm (Fig. 3D), and 17% of synapses had a PSD diameter larger than or equal to 315 nm. Whether these remaining large PSDs are attributable to incomplete knockdown, incomplete structural turnover, or some unknown compensatory processes at synapses remains unclear.

Contact area of a synapse, defined as the area of the postsynaptic membrane aligned with the presynaptic terminal, was measured from STEM tomography reconstructions of synapses where complete PSD areas were available. In contrast to the marked reduction in the size and area of PSDs, the contact area of the synaptic terminals was not significantly affected by knockdown: $0.25 \pm 0.16 \mu\text{m}^2$ ($n = 51$, control) and $0.21 \pm 0.15 \mu\text{m}^2$ ($n = 109$, knockdown; $P = 0.077$, NS), demonstrating that the knockdown reduces the areas of PSDs without concomitant structural changes in the membranes of pre- or postsynaptic terminals.

Analysis of Vertical Filaments at the PSD by EM Tomography.

Seventeen Lenti-KD-treated and 14 control spine synapses in rat hippocampal cultures were high-pressure frozen, freeze-substituted, and reconstructed at high resolution by EM tomography from 100- to 200-nm-thick sections. The tomograms were analyzed using established criteria for classifying the main structural elements at the PSD (3, 4, 37). Measurements on the core classes of structural elements, such as membrane-associated vertical filaments, revealed significant changes in their density and spatial organization following the MAGUK knockdown (Figs. 4 and 5).

Vertical filaments in controls (Fig. 4, red profiles) were uniformly distributed along the postsynaptic membrane at a density

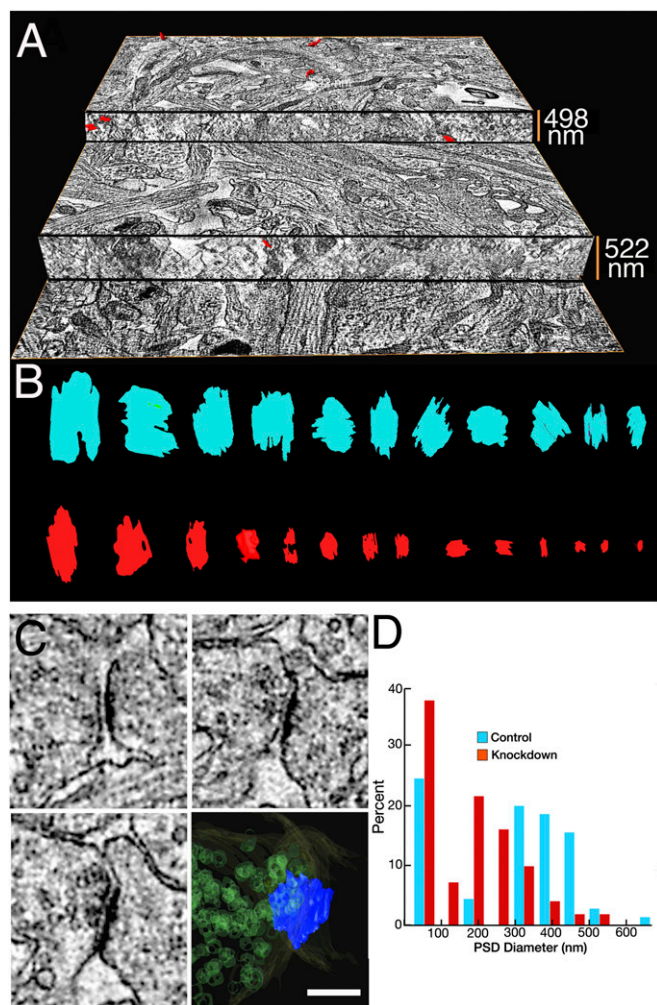


Fig. 3. Effect of triple-MAGUK knockdown on PSD length analyzed by STEM tomography. STEM tomography of micrometer thick plastic sections through hippocampal cultures allows entire PSDs to be rendered in 3D. (A) Exploded view of a tomogram with an $8.4 \times 8.4 \times 1.2 \mu\text{m}$ volume (8.2 nm per pixel; 1,024 \times 1,024 \times 147 voxel data volume) from a plastic section through a hippocampal culture after triple-MAGUK knockdown. Numbers on the right designate sizes of arbitrary steps cut out of the tomogram to illustrate its 3D character. Individual PSDs in reconstruction are surface-rendered in red. (B) En face projections of entire PSDs from control (cyan) and triple-MAGUK knockdown (red). (C) Virtual sections from three different levels of a STEM tomogram of a spine synapse with clearly identifiable electron-dense PSD material contained in the reconstructed 3D volume. Section numbers are as follows: 96 (C, Upper Left), 81 (C, Lower Left), and 73 (C, Upper Right) (8.2 nm/pixel). (C, Lower Right) Surface rendering of the same synapse: pre- and postsynaptic membrane (translucent yellow), presynaptic vesicle (translucent green), and PSD (solid blue). (Scale bar: 200 nm.) (D) Histogram comparing the distributions of PSD diameters in control and triple-MAGUK knockdown synapses.

$$\text{PSD diameter} = \sqrt{\frac{4 \times \text{PSD area}}{\pi}}$$

of $368 \pm 21/0.1 \mu\text{m}^2$ ($n = 5$ regions, control). Upon knockdown (Fig. 5), the distributions of vertical filaments, especially those located at the periphery of the PSD, became patchy and sparser, with their density reduced by $\sim 50\%$ to $187 \pm 85/0.1 \mu\text{m}^2$ ($n = 19$ regions, knockdown). The remaining vertical filaments usually associated with other structures, such as horizontal elements and transmembrane structures in the postsynaptic membrane (Fig. S3). Because measurements based on STEM tomography show a reduction of 68% in PSD area following knockdown, the

expected reduction in the total number of vertical filaments was 84%. The degree of depletion of vertical filaments suggests that they essentially correspond to the MAGUKs.

Analysis of AMPAR- and NMDAR-Type Structures by EM Tomography.

Two major classes of transmembrane structures seen in tomograms at the PSD were originally designated as AMPAR- or NMDAR-type, respectively (3), based on the close match between the sizes and shapes of their electron-dense structure in the synaptic cleft and the extracellular domains at high-resolution structures of AMPA and NMDA receptors (64–66). The corresponding cytoplasmic sides of these two types of transmembrane structures in tomograms differed markedly in size and shape, consistent with the fact that C-terminal tails of NMDA receptors, especially GluN2 C tails, are much larger than those of any of the AMPAR subunits (3, 4, 37, 67). The size of the NMDAR cytoplasmic domain is predicted to be about twice that of AMPARs (3). Indeed, immuno-EM labeling of the cytoplasmic side of AMPAR locates GluA2/3 at 2.9 nm, whereas GluN1 is located 5.1 nm from the membrane, indicating that NMDARs have a larger cytoplasmic domain than AMPARs (68). Thus, transmembrane structures with larger cytoplasmic aspects are tentatively designated as NMDAR-type structures (Figs. 4 and 5, cyan profiles), and those with a thin, flat cytoplasmic side are designated as AMPAR-type structures (blue profiles).

When segmented as transmembrane structures in tomograms, the extracellular sides of both AMPAR- and NMDAR-type structures are often associated with filaments crossing the synaptic cleft (3). The

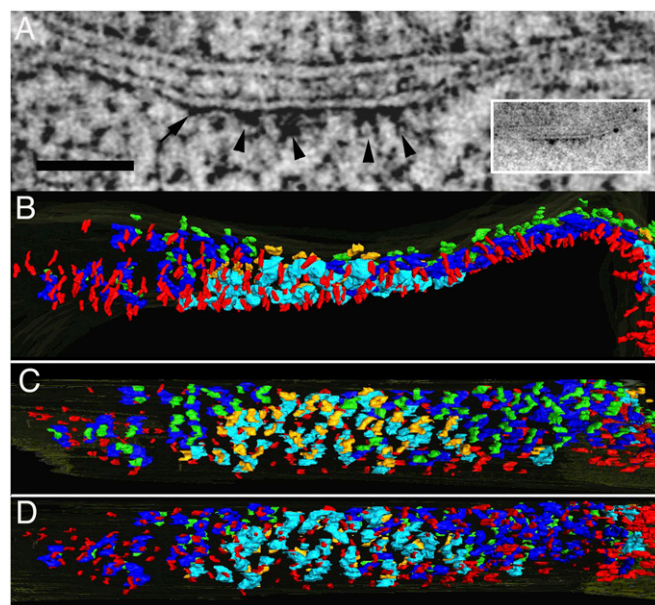


Fig. 4. Transmission electron tomography of the core structure of a PSD derived from ~ 100 -nm-thick section through a control hippocampal culture. (A) Single virtual section derived from tomogram; arrows point to slender AMPAR-type structure; arrowheads indicate cytoplasmic aspects of larger NMDAR-type structures. *Inset* shows appearance of PSD in ~ 100 -nm-thick section in a transmission EM (TEM) image. (Scale bars: 100 nm.) (B) Surface rendering of core elements of PSDs viewed in near cross-section. Red, vertical filaments on the inside surface of PSD; cyan, putative NMDA receptors; blue, putative AMPA receptors. (C) PSD rotated to show the outer surface in en face view; outer parts of the putative NMDA receptors are orange, and outer parts of the putative AMPA receptor are green. The membrane has been rendered as transparent, so the inner parts of the core structure can be shown. (D) PSD rotated, mirror-imaged to align with C and to show its inner surface en face; color coding is the same as described for B and C. Some of the gold and green on the outer aspects of the receptors shows through the transparent membrane.

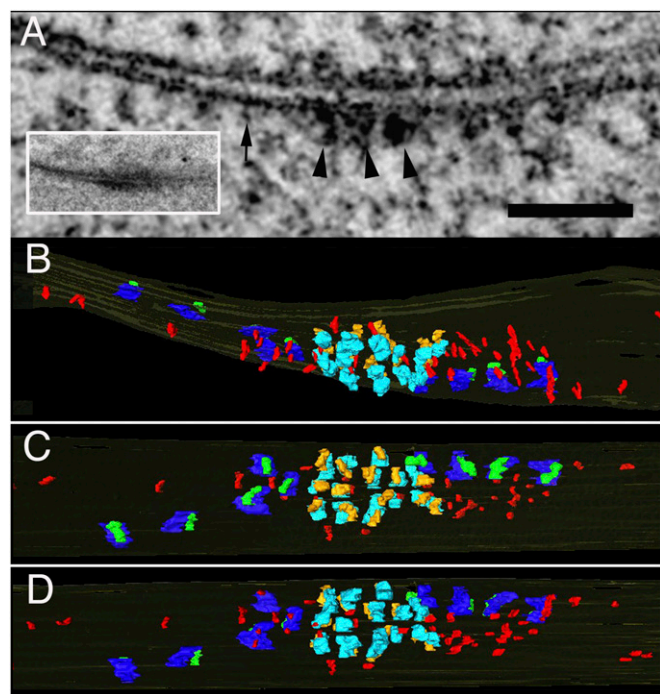


Fig. 5. A PSD from a spine synapse after triple-MAGUK knockdown shows marked depletion of vertical filaments and putative AMPAR-type structures (arrows) in the same set of views as in Fig. 4. (A) Inset shows TEM image of PSD in an ~100-nm section. (B–D) The putative NMDAR-type structures (arrowheads), in contrast to markedly depleted putative AMPAR-type structures, are still present in a centrally located cluster, albeit with much smaller cluster size than control in Fig. 4. (Scale bars: 100 nm.)

dimensions of the extracellular domains of AMPAR-type structures measured at the postsynaptic membrane were 14 ± 2 nm long, 6 ± 1 nm wide, and 6 ± 1 nm high ($n = 11$), and their corresponding cytoplasmic domains associated with the postsynaptic membrane were 20 ± 3 nm long, 11 ± 2 nm wide, and 4 ± 1 nm high ($n = 11$). The dimensions of extracellular domains of NMDAR-type structures were 15 ± 3 nm long, 7 ± 1 nm wide, and 7 ± 3 nm high ($n = 8$), and the dimensions of the corresponding cytoplasmic domains were 17 ± 3 nm long, 13 ± 3 nm wide, and 13 ± 4 nm high ($n = 8$; Figs. 4 and 5). In both control and knockdown groups, NMDAR-type structures form a 100- to 200-nm-diameter cluster centered in the PSD, whereas the AMPAR-type structures arrayed outside of the NMDAR cluster to occupy the rest of the PSD (Figs. 4 and 5). The distinct spatial distribution of these two types of structures closely matches the distributions of the two types of glutamate receptors in hippocampal CA1 dendritic spines reported by immuno-EM (8, 10).

Next, we determined the relationships of the numbers of AMPAR- or NMDAR-type structures to PSD diameter, both of which were measured from renderings of entire tomograms of partial segments of PSDs in thin sections. Because the synapses selected for tomography reconstructions were photographed in cross-section views, they often contain central regions of the PSD (Fig. 4), which allowed the PSD diameter to be estimated from the maximum PSD length in the main axis of the renderings of PSDs (Figs. 4 and 5). To gather data from a wide range of PSD sizes, reconstructions of PSDs ranging from small and large spine synapses were included (Fig. 6A and B). In controls, the number of AMPAR-type structures was linearly and positively correlated with the PSD diameter [$n = 14$, $r = 0.87$ (critical value, $r = 0.53$), $P < 0.001$; Fig. 6A]. The best-fit line had an intercept of 176 nm for the PSD diameter, below which the number of AMPAR-type structures at the PSD falls to zero (Fig. 6A). This number matched the ~180-nm minimum PSD-diameter threshold for AMPAR immunoactivity

found by serial-section immuno-EM (8). In contrast, the number of NMDAR-type structures (Fig. 6B), which remained approximately constant, was independent of the PSD diameter in controls [$n = 14$, $r = 0.22$ (critical value, $r = 0.53$), $0.2 < P < 0.5$]. These distinguishing properties of AMPAR- and NMDAR-type structures matched the properties of AMPARs and NMDARs at the PSD shown by immuno-EM (8, 10). Two-photon uncaging of glutamate on dendritic spines illustrated a similar dependence of AMPAR and NMDAR responses on spine size (69, 70). Thus, AMPAR-type and NMDAR-type structures, as classified by EM tomography, are coextensive with AMPARs and NMDARs, respectively. Synapses with PSD diameters around 176 nm are composed of an NMDAR cluster with a few or no AMPARs, consistent with functionally silent synapses (8).

The density of AMPAR-type structures in controls was $135 \pm 66 / 0.1 \mu\text{m}^2$ ($n = 5$; Figs. 4 and 6D and Table S1), and the estimated total number of AMPARs in an average size PSD was 105 ± 52 (Table S1). These numbers match the estimates of AMPARs based on glutamate uncaging (71) and freeze-fracture replica labeling (72). The number of NMDAR-type structures in controls in ~100-nm-thick slabs of PSDs is 23 ± 5 ($n = 12$), nearly a constant and independent of PSD size (Fig. 6B).

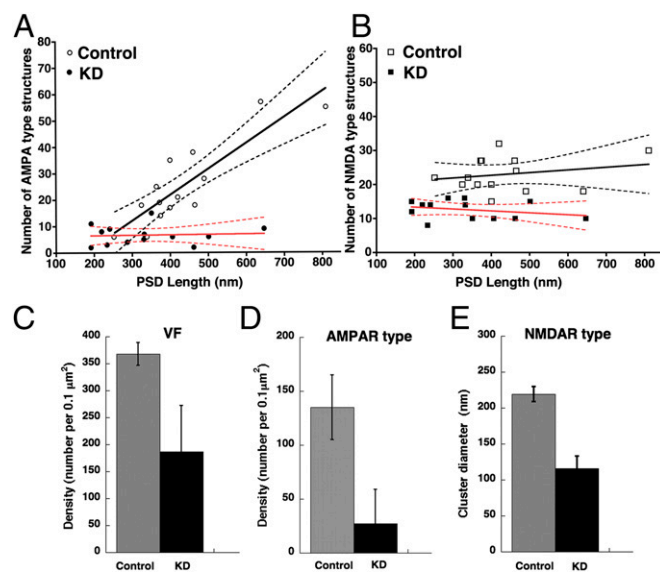


Fig. 6. Measurements of the triple-MAGUK knockdown effects on core structures in ~100-nm-thick sections of PSDs reconstructed by EM tomography. (A) Relationship between the number of AMPAR-type structures and maximum PSD length (PSD diameter) under control (open dots) and knockdown (dark dots) conditions. The control data fit to $y = 17.19 + 0.098x$ [solid black line; $r = 0.87$ (critical value, $r = 0.53$), $P < 0.001$] with the intercept of 176 nm in PSD diameter and is plotted with its 95% confidence interval (CI) lines (black dash lines). The AMPAR-type structure number is not correlated with PSD diameter following knockdown [$n = 13$, $r = 0.047$ (critical value, $r = 0.55$), $P > 0.5$], and the best-fit line (solid red line) is plotted with its 95% CI lines (dash red lines). (B) The number of NMDAR-type structures is independent of maximum PSD length (PSD diameter). Open squares represent control [$n = 14$, $r = 0.22$ (critical value, $r = 0.53$), $0.2 < P < 0.5$; the best-fit line and its 95% CI lines are black lines], and black squares represent knockdown [$n = 13$, $r = 0.28$ (critical value, $r = 0.55$), $0.2 < P < 0.5$; the best-fit line and its 95% CI lines are red lines]. The near-constant NMDAR number is 23 ± 5 ($n = 12$, control) and 12 ± 3 ($n = 12$, knockdown; $P < 0.0001$). NMDAR number is significantly reduced by knockdown. (C–E) Histograms comparing changes in density of vertical filaments at the reconstructed slabs of PSDs (C) and AMPAR-type structures (D) and sizes of clusters of NMDA-type structures (E) in control and triple-MAGUK knockdowns. VF designates vertical filaments, AMPA type designates AMPAR-type structures, and NMDA type designates NMDAR-type structures. All error bars are SDs.

Knockdown Reduces the Number of AMPAR-Type Structures. The number of AMPAR-type structures was greatly reduced and no longer correlated with PSD size [$n = 13$, $r = 0.047$ (critical value, $r = 0.55$), $P > 0.5$; Fig. 6A] following MAGUK knockdown, and AMPAR loss can be estimated by the reduction in the density of AMPAR at the PSD: the density of AMPARs was reduced to $27 \pm 32/0.1 \mu\text{m}^2$ ($n = 19$, $P < 0.0006$) (Figs. 5 and 6D). The $\sim 80\%$ reduction (Fig. 6D) aligns with the $\sim 74\%$ reduction in AMPAR EPSCs measured by electrophysiology (Fig. 1E1 and E2) and is also in agreement with the 84% reduction in the number of vertical filaments (Fig. 6C). AMPAR-type structures appeared to be relatively regularly spaced in control synapses at a nearest neighbor distance of $27 \pm 3 \text{ nm}$ [$n = 52$, control; coefficient of variation (CV) = 0.09], which increased upon knockdown to $49 \pm 61 \text{ nm}$ ($n = 72$, knockdown; CV = 1.26), with a much larger CV, indicating a marked reduction in the average of number AMPAR-type structures at the PSD and a significant increase in variation in the number of AMPARs at the PSD (Figs. 5 and 6). We also used another method by comparing the percentage reduction of AMPAR-type structures from the total number of AMPAR-type structures in $\sim 100\text{-nm}$ -thick slabs of PSDs reconstructed by EM tomography (Fig. 6A) under control and knockdown conditions. In an $\sim 400\text{-nm}$ -diameter PSD, the number of AMPAR-type structures sampled from slabs of PSDs decreased from 22 to 7 (Fig. 6A), corresponding to an $\sim 68\%$ reduction of AMPAR-type structures, which again fits the averaged EPSC reductions measured by electrophysiology.

We further examined by EM tomography the effects of knockdown on the number of AMPAR-type structures at the PSD. In contrast to controls, the number of AMPAR-type structures in the slabs of PSDs was reduced to a minimum baseline across all sizes of PSDs (Fig. 6A) with the lower limit of PSD diameter at less than 200 nm, approaching the 176 nm limit for silent synapses. The zones defined by 95% CI lines around best-fit lines from control and knockdown group overlapped for PSDs less than 250 nm in diameter such that AMPAR numbers in smaller PSDs from the knockdown group are indistinguishable from controls and counted for 7 out of 13 (54%) PSDs in the knockdown group. The results showed that the greatest loss of AMPARs is from larger PSDs on larger spines.

Knockdown Reduces the Number of NMDAR-Type Structures. The number of NMDAR-type structures is nearly a constant, independent of PSD size, in knocked down synapses [$n = 13$, $r = 0.28$ (critical value, $r = 0.55$), $0.2 < P < 0.5$]. The total number of NMDAR-type structures in slabs of $\sim 100\text{-nm}$ -thick PSDs was 23 ± 5 ($n = 12$ control) and 12 ± 3 ($n = 12$, knockdown, $P < 0.0001$), respectively, indicative of an $\sim 50\%$ reduction in numbers of NMDAR-type structures following the knockdown (Fig. 6B), which is in-line with the expected $\sim 60\%$ reduction from electrophysiological measurements (Fig. 1F). Individual NMDAR-type structures appeared to form a lattice-like cluster located more centrally in the PSD (Figs. 4 and 5). The NMDAR-type structures were arrayed at a nearly the same nearest neighbor distances in control and knockdown groups: $30 \pm 2 \text{ nm}$ ($n = 63$; 3 synapses, control) and $31 \pm 5 \text{ nm}$ ($n = 197$; 13 synapses, knockdown; one-way ANOVA, $P = 0.693$). Alternatively, we estimated NMDAR reduction from the shrinkage of the central NMDAR cluster size at the PSD. The average diameter of NMDAR clusters, measured from the major axis of the NMDAR cluster at the membrane, was $220 \pm 10 \text{ nm}$ ($n = 3$, control) but was reduced by $\sim 50\%$ following knockdown to $116 \pm 17 \text{ nm}$ ($n = 12$, knockdown; one-way ANOVA, $P < 0.0001$). Given the constant NMDAR nearest neighbor distance and the $\sim 50\%$ reduction in the diameter of NMDAR clusters, these resulting changes would correspond to an $\sim 75\%$ reduction in the number of NMDAR-type structures upon knockdown, in agreement with the level of reduction in NMDAR EPSCs. Thus, NMDAR-type structures are significantly reduced by MAGUK knockdown.

Discussion

The mechanisms by which glutamate receptors are anchored and retained at the PSD are critically important for understanding the molecular basis of synaptic transmission and plasticity (5, 11, 73). It is becoming clear that the MAGUK proteins have a central role in maintaining and anchoring glutamate receptors at the PSD (54). Here, we combined electrophysiological recording and advanced EM to evaluate the effects of simultaneous knockdown of three major MAGUK proteins on both synaptic function and the molecular organization of the PSD.

Analyses of high-resolution TEM tomograms reveals detailed molecular-level images of the organization of key elements at the PSD (3, 4, 67). Reconstructions of the entire PSD by STEM tomography on thick sections (62, 63) helps to evaluate the global effects of the knockdown on the sizes of PSDs and synaptic terminals. Data from electrophysiology and thin- and thick-section EM tomography illustrate how MAGUKs play essential roles in maintaining the overall morphology of the PSD and in anchoring glutamate receptors at the PSD (Fig. 7 and Table S1).

Functional Consequences of Triple MAGUK Knockdown. MAGUKs are required for the localization of both AMPARs and NMDARs at synapses (30, 54), but single-MAGUK knockdown mainly causes loss of AMPAR transmission (30, 32). AMPARs are selectively lost following a modest decrease in MAGUKs, but both classes of glutamate receptor are anchored at the PSD by MAGUKs, as demonstrated by triple-MAGUK knockdown in slice cultures (54) and in dissociated cultures in the present study. Electrophysiology showed a modest decrease in mEPSC size and a considerably larger decrease in mEPSC frequency (Fig. 1G and J). How do these physiological results compare with the anatomical results? The large decrease in frequency is consistent with the dramatic loss of AMPARs. With the loss of AMPARs, one would expect that many of the mEPSC events would fall below the detection threshold (Fig. S2). However, we were surprised not to see a greater reduction in mEPSC amplitude, given the large reduction in the number of AMPARs at larger synapses, and have no definitive explanation for this difference.

How do the present results with AMPARs compare with our previous results in slice culture (53)? As in the present study, we found previously that triple-MAGUK knockdown caused a large decrease in the frequency of mEPSC events. However, no change in the amplitude of the remaining events was seen. This was surprising, given that MAGUKs are present at all synapses. We presented evidence that during the MAGUK knockdown, there is initially a uniform loss of AMPARs across all synapses, and that over a period of days, a process we term consolidation takes place, where most synapses go entirely silent and the few remaining synapses acquire their normal complement of AMPARs (54). We interpret the difference between these two studies to mean that the

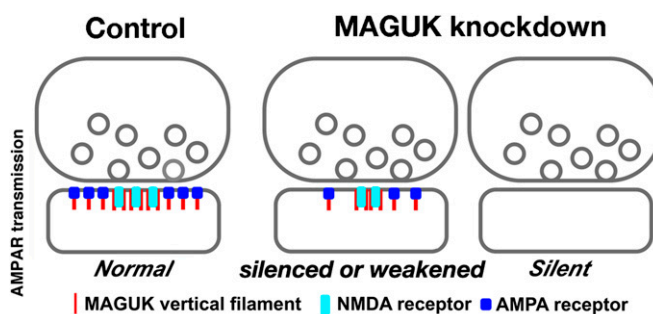


Fig. 7. MAGUK knockdown decimates the core structure at the PSD. The schematic illustrates the consequences of MAGUK knockdown, based on combined data from electrophysiology and TEM and STEM tomography.

process of consolidation is incomplete in dissociated neurons compared with slice culture. The present anatomical results with NMDARs suggest a uniform reduction in the number of NMDARs across all synapses. This finding is clearly different from our previous results in slice culture where we presented evidence for an all-or-none loss of NMDARs. Further research is required to determine the underlying differences between these two preparations.

Identification of AMPAR and NMDAR Complexes. Two types of transmembrane structures with distinct morphologies at the PSD revealed by EM tomography analysis showed shapes and sizes and copy numbers and distributions consistent with those of AMPAR and NMDAR complexes. The following key findings support their identification. (i) The two types of structures and the two types of receptors at the PSD–NMDARs are generally located in the central region of the PSD, whereas AMPARs occupy the peripheral regions of the PSD (8, 10). (ii) The number of AMPAR-type structures is positively correlated with PSD size, and the number of NMDAR-type structures is independent of PSD size, in agreement with the results from other methods such as serial-section immuno-EM (8, 10) and two-photon uncaging of glutamate on dendritic spines (69–71). (iii) The 176-nm diameter of the central NMDAR cluster at PSDs from this work matches the minimum PSD diameter of ~180 nm for PSDs lacking AMPARs (8). Thus, a class of smaller spines composed of a NMDAR cluster devoid of or containing very few AMPARs appears to correspond with silent synapses (8). (iv) The estimated numbers of glutamate receptors: ~100 AMPAR-type and 20–30 NMDAR-type structures per PSD based on tomography match closely the number of AMPARs and NMDARs at synapses estimated by electrophysiology (71, 74), biochemistry and mass spectrometry (12, 75), two-photon imaging (76), and freeze-fracture immunolabeling (72). (v) The losses of the two types of receptor structures upon knockdown (Table S1) track the losses of synaptic transmission mediated by the two types of glutamate receptors. For these five reasons, we conclude that AMPAR- or NMDAR-type structures revealed by EM tomography correspond with or at least contain AMPAR or NMDAR complexes. The differential radial organization of AMPARs and NMDARs, however, may be limited to synapses in hippocampus (8, 10) and in cerebral cortex (6), because these receptors are not segregated in other brain regions (77).

Structural Consequences of Triple-MAGUK Knockdown. Knockdown of PSD-95 alone results in deletion of small patches of PSD up to 100 nm in diameter (37). Triple-MAGUK knockdown, in contrast, is associated with a significant reduction in the overall PSD size, as was evident both in 2D analyses by conventional thin-section EM and in 3D analyses by STEM tomography. The areas of contact between the pre- and postsynaptic membranes remained unaffected, and neither spine size nor the arrangements of presynaptic active zones appeared to be significantly altered. This conclusion is consistent with a previous finding that spine volume is not changed in PSD-95 KO mice (29). In contrast to the incorporation of PSD-95 leading to maturation and enlargement of spines (78), the loss of correlation between PSD area and spine size following knockdown indicates that some of the larger spines have lost a significantly larger portion of their electron-dense PSDs than smaller spines, suggesting that the loss in larger PSDs can be attributed to MAGUKs. Both 2D thin-section EM analysis and 3D STEM tomography showed that a subpopulation of synapses (~20%) lost their entire PSDs, whereas the remaining synapses show a loss of ~70% in PSD area. The synapses lacking typical PSDs were at low abundance in controls but increased significantly following MAGUK knockdown, suggesting that these synapses represent immature excitatory synapses. These data show that, at least in some populations of the synapses, MAGUKs are the structural determinant in maintaining the electron-dense layer of the PSD (59, 79). The fact that the presynaptic side of the synapse appears intact after MAGUK knockdown suggests that MAGUKs might

not be critical for localization of postsynaptic cell adhesion molecules, such as the neuroligins (80). It is now feasible to examine proteins in the synaptic cleft following MAGUK knockdown (81).

Knockdown Depletes Vertical Filaments at the PSD. Reconstruction of the core PSD structures by EM tomography reveals a prominent class of membrane-associated vertical filaments that associate with transmembrane structures and with horizontal elements (3, 4, 37, 67). The vertical filaments appear to be essential to the assembly of the PSD because their elimination can potentially lead to disassembly of entire segments of the core PSD structure (3, 37). The suggestion that vertical filaments contain PSD-95 (3) is thus far supported by several lines of evidences: positive labeling of the vertical filament for PSD-95 (3, 4, 37, 67); distinct orientation of N and C termini of PSD-95 relative to the postsynaptic membrane (37); close matching of length (16–20 nm) of the vertical filaments with expected length of an extended PSD-95 or SAP97 molecule (3, 37); close matching of their density of $368/0.1 \mu\text{m}^2$ to the copy number of PSD-95 family proteins in the PSD (51, 52, 75); and loss of vertical filaments upon knockdown of PSD-95 (37).

Here, we demonstrate that when all three MAGUKs are knocked down, ~20% or more synapses completely lack an electron-dense PSD, including vertical filaments, whereas the remaining synapses show an 84% reduction in the number of vertical filaments (Figs. 5 and 6C). These data link most vertical filaments to MAGUKs. Although MAGUKs appear to dominate in the vertical filaments at the PSD, some members of the MAGUK family might contribute to the horizontal filaments associated with vertical filaments, because some MAGUKs can multimerize (5).

MAGUK Knockdown Depletes both AMPARs and NMDARs. Partial knockdown of PSD-95 results in an ~36% reduction in the number of vertical filaments and a concomitant ~33% reduction in AMPAR-type structures without apparent changes in the clustering of NMDAR-type structures (37). The triple-MAGUK knockdown results in an 84% reduction in the number of vertical filaments and a 70–80% reduction in the number of AMPAR-type structures. The almost identical extent of reductions in the number of vertical filaments and AMPAR-type structures provides evidence that MAGUKs in vertical filaments are the main structural proteins for anchoring and retaining AMPAR complexes at the PSD (82). These results also suggest a fixed stoichiometry between MAGUKs and AMPARs, perhaps via AMPAR-associated complexes such as Stargazin/TARPs (83).

Compared with partial PSD-95 knockdown, where NMDARs are not affected (37), the triple-MAGUK knockdown depleted NMDARs, but the extent of the knockdown effect on NMDAR-type structures appears different from that on AMPAR-type structures. NMDAR-type structures still form a central, albeit much smaller cluster at the PSD, while maintaining the same lattice spacing as in the control. In contrast, the MAGUK knockdown depletes the AMPARs at the periphery of the PSD, along with the vertical filaments that appear to anchor them at the PSD. These data show the relative stability of the NMDAR complex compared with AMPAR complexes. Although MAGUKs in vertical filaments are critical for anchoring AMPARs at the PSD, they may be necessary but not sufficient for anchoring NMDARs. Other proteins may well be involved in retaining the NMDAR complexes and in maintaining the complexes' more stable and regularly spaced lattice-like organization at the PSD. Surprisingly, in contrast to physiological findings in slice culture, where the loss of NMDARs appears to be all-or-none (54), the present results in dissociated culture appear to be graded, suggesting differences between these two neuronal preparations.

Integration of the Functional and Anatomical Observations. Electrophysiological measurements show a significant reduction of AMPAR mEPSC frequency and a relatively small but significant reduction in mEPSC amplitude (Fig. 1 *H1–J2*) following MAGUK knockdown.

Thus, there is a reduction in functional synapses containing AMPARs. Thin-section EM and STEM tomography show that a subpopulation of synapses lose their entire PSDs, consistent with the reduction of AMPAR mEPSC frequency. The reduction in the size of the remaining mEPSCs is consistent with a partial loss of AMPARs from the PSD. This reduction in the number of AMPARs at the remaining synapses would be expected to reduce the number of mEPSCs that reach the detection threshold for mEPSC analysis (Fig. S2), which in turn would contribute to the large reduction in mEPSC frequency. Quantitatively, the 75% reduction in AMPAR EPSC roughly matches the reduction in the number of AMPAR type of structures. The NMDAR-mediated current and the number of NMDAR type of structures are similarly reduced by quantitatively similar amounts, roughly 60%.

In summary, at the detailed molecular level afforded by advanced EM, the complete loss of the PSD in a subpopulation of synapses and the 84% loss of their vertical filaments provide direct evidence that reduction in synaptic transmission by MAGUK knockdown is tied to the elimination of the vertical filaments at the PSD. Furthermore, the association of this loss of vertical filaments with a reduction in AMPAR and NMDAR complexes and a reduction in glutamatergic synaptic transmission demonstrates the key roles for MAGUKs in anchoring AMPARs and NMDARs. The loss of synaptic transmission is largely attributable to the primary loss of MAGUKs that anchor postsynaptic glutamate receptors, which is then followed by losses of receptors from the PSD. Thus, the vertically oriented arrays of MAGUKs appearing as vertical filaments at the PSD provide the backbone structure for molecular assembly and maintenance of the PSD.

Materials and Methods

This work is approved by the University of California San Francisco and the National Institute of Neurological Disorders and Stroke (NINDS)/The National Institute on Deafness and Other Communication Disorders (NIDCD)/The National Center for Complementary and Integrative Health (NCCIH) Animal Care and Use Committees (ACUC).

Electrophysiology. Electrophysiological recordings were performed at 16 days in vitro (DIV16) to DIV21 at room temperature using borosilicate glass electrodes. External solution contained (in mM) 119 NaCl, 2.5 KCl, 4 CaCl₂, 4 MgSO₄, 1 NaH₂PO₄, 26.2 NaHCO₃, and 11 glucose and was bubbled continuously with 95% O₂/5% CO₂ (vol/vol). To block inhibitory currents, 100 μM picrotoxin was added, and to block evoked activity during mEPSC experiments, 0.5–1 μM TTX was added. Internal solution contained (in mM) 115 CsMeSO₃, 20 CsCl, 10 Hepes, 2.5 MgCl₂, 0.6 EGTA, 5 QX314-Cl (lidocaine N-ethyl chloride), 4 MgATP, 0.4 Na₃GTP, and 0.1 spermine. For measurement of evoked EPSCs, a bipolar stimulation electrode with 110-μm tip spacing (FHC) was gently touched to the culture coverslip 300–500 μm from the neuron pair oriented such that neurons were equidistant from the electrode. EPSCs were evoked at 0.1–0.2 Hz. Peak AMPAR currents were measured at –70 mV, and NMDAR currents were measured at +40 mV, 100 ms after stimulation. For aEPSC measurements, CaCl₂ was replaced by equimolar SrCl₂, and aEPSCs were evoked by trains of three pulses at 2 Hz. aEPSCs were obtained from DIV8–DIV9 organotypic slices prepared and maintained as previously described (23). mEPSCs and aEPSCs were analyzed offline with customized software (IGOR).

Transfection of Hippocampal Cultures for Electrophysiology. Dissociated rat hippocampal neurons [embryonic day 20 (E20)] were sparsely transfected at DIV4–DIV7 with Lipofectamine 2000 (Life Technologies). Briefly, 0.2 μL of Lipofectamine and 0.2 μg of DNA were mixed in 50 μL of Opti-mem (Life

Technologies) per well following the manufacturer's guidelines. Neurons were then incubated in Opti-mem transfection medium for 2–3 h. Transfection medium was aspirated, followed by 1× rinse with warm PBS and replacement with fresh warm conditioned medium.

Lentivirus Infection of Hippocampal Cultures for EM. Dissociated rat hippocampal neurons (E20) were plated on confluent glia layers, either on 35-mm coverslips for conventional EM and immuno-EM or in 3-mm gold specimen chambers for high-pressure freezing (3, 4, 67). Cultures were maintained in 10% CO₂ at 35 °C in custom MEM (Invitrogen) supplemented with 2 mM Glutamax 1 (Invitrogen), N3 (a growth factor mixture containing apo-transferrin, putrescine, selenium, triiodothyronine, insulin, progesterone, and corticosterone), 2% FBS (Invitrogen), and 5% horse serum (HyClone) in a HeraCell incubator (4, 84). Aliquots (5–10 μL) of high-titer virus (~10⁸/mL) were added to DIV5 hippocampal cultures, either on coverslips or in gold specimen chambers, and inoculated until DIV21 before high-pressure freezing or fixation for conventional or immuno-EM.

Preparation for Conventional and Immunogold EM. For morphological studies using conventional EM and STEM tomography, the cultures were fixed in freshly made glutaraldehyde at room temperature and subsequently washed before further EM processing. To identify knockdown-affected PSDs in spines, GFP antibody was used to immunogold label GFP reporters in Lenti-GFP (control) and Lenti-KD-GFP (knockdown). Details on fixing cells, immunogold labeling, and further EM processing (4, 37) are in *SI Materials and Methods*.

High-Pressure Freezing and Freeze Substitution. Cultures grown in gold specimen chambers were high-pressure frozen at 2,100 bar with a Bal-Tec high-pressure freezing machine (HPM) 010 followed with a freeze-substitution and low-temperature embedding protocol, as described previously (3, 4) and in detail in *SI Material and Methods*. Blocks are stored in a pumped desiccator for a several days before sectioning.

Conventional EM, Thick-Section STEM Tomography, and High-Resolution Transmission EM Tomography. Conventional EM data acquisition on ~80-nm-thick sections was performed with a JEOL 200CX electron microscope. Dual-axis TEM tomograms were acquired from 100- to 200-nm-thick Lowicryl sections, and dual-axis STEM tomograms were acquired from 1- to 2-μm-thick Epon sections at a beam energy of 300 keV using a field electron and ion (FEI) Tecnai TF30 transmission electron microscope equipped with a field emission gun (details are in *SI Materials and Methods*). For analysis of conventional EM images, measurements were done offline, blinded by a second investigator. All measurements are reported as means ± SD unless otherwise indicated.

Analysis of STEM and TEM Tomograms. For STEM tomography data analysis, PSD diameters are derived from the segmented and rendered PSD areas measured in Amira (FEI) (for details, see *SI Materials and Methods*). For TEM tomography data analysis, all core structural elements are classified, rendered, and counted according to previously published criteria (3, 4, 67). The density of a particular structure is calculated by counting its number divided by the postsynaptic membrane area it occupied (details are in *SI Materials and Methods*). All statistical analyses were performed with KaleidaGraph (Synergy) and Prism (GraphPad).

ACKNOWLEDGMENTS. We thank Susan Cheng and Virginia Crocker of the National Institute of Neurological Disorders and Stroke (NINDS) EM facility for their support with immunogold EM and EM processing, Carolyn Smith and Paul Gallant of the NINDS light microscopy imaging facility for their help with confocal microscopy, Harold Gainer and Ray Fields for providing a facility for lentivirus-related work, John Chludzinski and Daniel Cox for help with data analysis, and Andy Jan and Austin Feng for critical reading of the manuscript. This work was supported by intramural funds from NINDS and National Institute of Biomedical Imaging and Bioengineering of the NIH and NIH grants (to R.A.N.).

- Palay SL (1956) Synapses in the central nervous system. *J Biophys Biochem Cytol* 2 (4 Suppl):193–202.
- Kennedy MB (2000) Signal-processing machines at the postsynaptic density. *Science* 290(5492):750–754.
- Chen X, et al. (2008) Organization of the core structure of the postsynaptic density. *Proc Natl Acad Sci USA* 105(11):4453–4458.
- Chen X, et al. (2014) *Nanoscale Imaging of Protein Molecules at the Postsynaptic Density* (Springer Science+Business Media, New York).
- Sheng M, Kim E (2011) The postsynaptic organization of synapses. *Cold Spring Harb Perspect Biol* 3(12):a005678.
- Kharazia VN, Weinberg RJ (1997) Tangential synaptic distribution of NMDA and AMPA receptors in rat neocortex. *Neurosci Lett* 238(1-2):41–44.
- Valtschanoff JG, Weinberg RJ (2001) Laminar organization of the NMDA receptor complex within the postsynaptic density. *J Neurosci* 21(4):1211–1217.
- Takumi Y, Ramirez-León V, Laake P, Rinivik E, Ottersen OP (1999) Different modes of expression of AMPA and NMDA receptors in hippocampal synapses. *Nat Neurosci* 2(7):618–624.
- Nusser Z, et al. (1998) Cell type and pathway dependence of synaptic AMPA receptor number and variability in the hippocampus. *Neuron* 21(3):545–559.
- Racca C, Stephenson FA, Streit P, Roberts JD, Somogyi P (2000) NMDA receptor content of synapses in stratum radiatum of the hippocampal CA1 area. *J Neurosci* 20(7):2512–2522.

11. Brecht DS, Nicoll RA (2003) AMPA receptor trafficking at excitatory synapses. *Neuron* 40(2):361–379.
12. Cheng D, et al. (2006) Relative and absolute quantification of postsynaptic density proteome isolated from rat forebrain and cerebellum. *Mol Cell Proteomics* 5(6):1158–1170.
13. Lowenthal MS, Markey SP, Dosemeci A (2015) Quantitative mass spectrometry measurements reveal stoichiometry of principal postsynaptic density proteins. *J Proteome Res* 14(6):2528–2538.
14. Cho KO, Hunt CA, Kennedy MB (1992) The rat brain postsynaptic density fraction contains a homolog of the *Drosophila* discs-large tumor suppressor protein. *Neuron* 9(5):929–942.
15. Kim E, Cho KO, Rothschild A, Sheng M (1996) Heteromultimerization and NMDA receptor-clustering activity of Chapsyn-110, a member of the PSD-95 family of proteins. *Neuron* 17(1):103–113.
16. Niethammer M, Kim E, Sheng M (1996) Interaction between the C terminus of NMDA receptor subunits and multiple members of the PSD-95 family of membrane-associated guanylate kinases. *J Neurosci* 16(7):2157–2163.
17. Müller BM, et al. (1996) SAP102, a novel postsynaptic protein that interacts with NMDA receptor complexes in vivo. *Neuron* 17(2):255–265.
18. Kim E, Sheng M (2004) PDZ domain proteins of synapses. *Nat Rev Neurosci* 5(10):771–781.
19. Doyle DA, et al. (1996) Crystal structures of a complexed and peptide-free membrane protein-binding domain: Molecular basis of peptide recognition by PDZ. *Cell* 85(7):1067–1076.
20. Long JF, et al. (2003) Supramolecular structure and synergistic target binding of the N-terminal tandem PDZ domains of PSD-95. *J Mol Biol* 327(1):203–214.
21. McGee AW, et al. (2001) Structure of the SH3-guanylate kinase module from PSD-95 suggests a mechanism for regulated assembly of MAGUK scaffolding proteins. *Mol Cell* 8(6):1291–1301.
22. Kornau HC, Schenker LT, Kennedy MB, Seeburg PH (1995) Domain interaction between NMDA receptor subunits and the postsynaptic density protein PSD-95. *Science* 269(5231):1737–1740.
23. Schnell E, et al. (2002) Direct interactions between PSD-95 and stargazin control synaptic AMPA receptor number. *Proc Natl Acad Sci USA* 99(21):13902–13907.
24. Chen L, et al. (2000) Stargazin regulates synaptic targeting of AMPA receptors by two distinct mechanisms. *Nature* 408(6815):936–943.
25. Nicoll RA, Tomita S, Brecht DS (2006) Auxiliary subunits assist AMPA-type glutamate receptors. *Science* 311(5765):1253–1256.
26. Bats C, Groc L, Choquet D (2007) The interaction between PSD-95 and PSD-95 regulates AMPA receptor surface trafficking. *Neuron* 53(5):719–734.
27. MacGillavry HD, Song Y, Raghavachari S, Blanpied TA (2013) Nanoscale scaffolding domains within the postsynaptic density concentrate synaptic AMPA receptors. *Neuron* 78(4):615–622.
28. Nair D, et al. (2013) Super-resolution imaging reveals that AMPA receptors inside synapses are dynamically organized in nanodomains regulated by PSD95. *J Neurosci* 33(32):13204–13224.
29. Béique JC, et al. (2006) Synapse-specific regulation of AMPA receptor function by PSD-95. *Proc Natl Acad Sci USA* 103(51):19535–19540.
30. Elias GM, et al. (2006) Synapse-specific and developmentally regulated targeting of AMPA receptors by a family of MAGUK scaffolding proteins. *Neuron* 52(2):307–320.
31. Schlüter OM, Xu W, Malenka RC (2006) Alternative N-terminal domains of PSD-95 and SAP97 govern activity-dependent regulation of synaptic AMPA receptor function. *Neuron* 51(1):99–111.
32. Ehrlich I, Klein M, Rumpel S, Malinow R (2007) PSD-95 is required for activity-driven synapse stabilization. *Proc Natl Acad Sci USA* 104(10):4176–4181.
33. Craven SE, El-Husseini AE, Brecht DS (1999) Synaptic targeting of the postsynaptic density protein PSD-95 mediated by lipid and protein motifs. *Neuron* 22(3):497–509.
34. Topinka JR, Brecht DS (1998) N-terminal palmitoylation of PSD-95 regulates association with cell membranes and interaction with K⁺ channel Kv1.4. *Neuron* 20(1):125–134.
35. El-Husseini Ael-D, et al. (2002) Synaptic strength regulated by palmitate cycling on PSD-95. *Cell* 108(6):849–863.
36. Sturgill JF, Steiner P, Czervionke BL, Sabatini BL (2009) Distinct domains within PSD-95 mediate synaptic incorporation, stabilization, and activity-dependent trafficking. *J Neurosci* 29(41):12845–12854.
37. Chen X, et al. (2011) PSD-95 is required to sustain the molecular organization of the postsynaptic density. *J Neurosci* 31(17):6329–6338.
38. Nakagawa T, et al. (2004) Quaternary structure, protein dynamics, and synaptic function of SAP97 controlled by L27 domain interactions. *Neuron* 44(3):453–467.
39. Jeyifous O, et al. (2009) SAP97 and CASK mediate sorting of NMDA receptors through a previously unknown secretory pathway. *Nat Neurosci* 12(8):1011–1019.
40. Howard MA, Elias GM, Elias LA, Swat W, Nicoll RA (2010) The role of SAP97 in synaptic glutamate receptor dynamics. *Proc Natl Acad Sci USA* 107(8):3805–3810.
41. Naisbitt S, et al. (1997) Characterization of guanylate kinase-associated protein, a postsynaptic density protein at excitatory synapses that interacts directly with postsynaptic density-95/synapse-associated protein 90. *J Neurosci* 17(15):5687–5696.
42. Kim E, et al. (1997) GKAP, a novel synaptic protein that interacts with the guanylate kinase-like domain of the PSD-95/SAP90 family of channel clustering molecules. *J Cell Biol* 136(3):669–678.
43. Naisbitt S, et al. (1999) Shank, a novel family of postsynaptic density proteins that binds to the NMDA receptor/PSD-95/GKAP complex and cortactin. *Neuron* 23(3):569–582.
44. Tu JC, et al. (1999) Coupling of mGluR/Homer and PSD-95 complexes by the Shank family of postsynaptic density proteins. *Neuron* 23(3):583–592.
45. Sala C, et al. (2001) Regulation of dendritic spine morphology and synaptic function by Shank and Homer. *Neuron* 31(1):115–130.
46. Bhattacharyya S, Biou V, Xu W, Schlüter O, Malenka RC (2009) A critical role for PSD-95/AKAP interactions in endocytosis of synaptic AMPA receptors. *Nat Neurosci* 12(2):172–181.
47. Xu W, et al. (2008) Molecular dissociation of the role of PSD-95 in regulating synaptic strength and LTD. *Neuron* 57(2):248–262.
48. Kim E, Niethammer M, Rothschild A, Jan YN, Sheng M (1995) Clustering of Shaker-type K⁺ channels by interaction with a family of membrane-associated guanylate kinases. *Nature* 378(6552):85–88.
49. Futai K, et al. (2007) Retrograde modulation of presynaptic release probability through signaling mediated by PSD-95-neurologin. *Nat Neurosci* 10(2):186–195.
50. Irie M, et al. (1997) Binding of neurologins to PSD-95. *Science* 277(5331):1511–1515.
51. Chen X, et al. (2005) Mass of the postsynaptic density and enumeration of three key molecules. *Proc Natl Acad Sci USA* 102(32):11551–11556.
52. Sugiyama Y, Kawabata I, Sobue K, Okabe S (2005) Determination of absolute protein numbers in single synapses by a GFP-based calibration technique. *Nat Methods* 2(9):677–684.
53. Sheng M (2001) Molecular organization of the postsynaptic specialization. *Proc Natl Acad Sci USA* 98(13):7058–7061.
54. Levy JM, Chen X, Reese TS, Nicoll RA (2015) Synaptic consolidation normalizes AMPAR quantal size following MAGUK loss. *Neuron* 87(3):534–548.
55. Maximov A, Pang ZP, Tervo DG, Südhof TC (2007) Monitoring synaptic transmission in primary neuronal cultures using local extracellular stimulation. *J Neurosci Methods* 161(1):75–87.
56. Xu-Friedman MA, Regehr WG (2000) Probing fundamental aspects of synaptic transmission with strontium. *J Neurosci* 20(12):4414–4422.
57. Mileti R (1966) Strontium as a substitute for calcium in the process of transmitter release at the neuromuscular junction. *Nature* 212(5067):1233–1234.
58. Oliet SH, Malenka RC, Nicoll RA (1996) Bidirectional control of quantal size by synaptic activity in the hippocampus. *Science* 271(5253):1294–1297.
59. Petersen JD, et al. (2003) Distribution of postsynaptic density (PSD)-95 and Ca²⁺/calmodulin-dependent protein kinase II at the PSD. *J Neurosci* 23(35):11270–11278.
60. Harris KM, Stevens JK (1989) Dendritic spines of CA 1 pyramidal cells in the rat hippocampus: Serial electron microscopy with reference to their biophysical characteristics. *J Neurosci* 9(8):2982–2997.
61. Meyer D, Bonhoeffer T, Scheuss V (2014) Balance and stability of synaptic structures during synaptic plasticity. *Neuron* 82(2):430–443.
62. Hohmann-Marriott MF, et al. (2009) Nanoscale 3D cellular imaging by axial scanning transmission electron tomography. *Nat Methods* 6(10):729–731.
63. Sousa AA, Azari AA, Zhang G, Leapman RD (2011) Dual-axis electron tomography of biological specimens: Extending the limits of specimen thickness with bright-field STEM imaging. *J Struct Biol* 174(1):107–114.
64. Sobolevsky AI, Rosconi MP, Gouaux E (2009) X-ray structure, symmetry and mechanism of an AMPA-subtype glutamate receptor. *Nature* 462(7274):745–756.
65. Nakagawa T, Cheng Y, Ramm E, Sheng M, Walz T (2005) Structure and different conformational states of native AMPA receptor complexes. *Nature* 433(7025):545–549.
66. Lee CH, et al. (2014) NMDA receptor structures reveal subunit arrangement and pore architecture. *Nature* 511(7508):191–197.
67. Chen X, Winters CA, Reese TS (2008) Life inside a thin section: Tomography. *J Neurosci* 28(38):9321–9327.
68. Kharazia VN, Weinberg RJ (1999) Immunogold localization of AMPA and NMDA receptors in somatic sensory cortex of albino rat. *J Comp Neurol* 412(2):292–302.
69. Sobczyk A, Scheuss V, Svoboda K (2005) NMDA receptor subunit-dependent [Ca²⁺]_i signaling in individual hippocampal dendritic spines. *J Neurosci* 25(26):6037–6046.
70. Zito K, Scheuss V, Knott G, Hill T, Svoboda K (2009) Rapid functional maturation of nascent dendritic spines. *Neuron* 61(2):247–258.
71. Matsuzaki M, et al. (2001) Dendritic spine geometry is critical for AMPA receptor expression in hippocampal CA1 pyramidal neurons. *Nat Neurosci* 4(11):1086–1092.
72. Masugi-Tokita M, Shigemoto R (2007) High-resolution quantitative visualization of glutamate and GABA receptors at central synapses. *Curr Opin Neurobiol* 17(3):387–393.
73. Elias GM, Nicoll RA (2007) Synaptic trafficking of glutamate receptors by MAGUK scaffolding proteins. *Trends Cell Biol* 17(7):343–352.
74. Bekkers JM, Stevens CF (1989) NMDA and non-NMDA receptors are co-localized at individual excitatory synapses in cultured rat hippocampus. *Nature* 341(6239):230–233.
75. Sheng M, Hoogenraad CC (2007) The postsynaptic architecture of excitatory synapses: A more quantitative view. *Annu Rev Biochem* 76:823–847.
76. Nimchinsky EA, Yasuda R, Oertner TG, Svoboda K (2004) The number of glutamate receptors opened by synaptic stimulation in single hippocampal spines. *J Neurosci* 24(8):2054–2064.
77. Bernard V, Bolam JP (1998) Subcellular and subsynaptic distribution of the NR1 subunit of the NMDA receptor in the neostriatum and globus pallidus of the rat: Colocalization at synapses with the GluR2/3 subunit of the AMPA receptor. *Eur J Neurosci* 10(12):3721–3736.
78. El-Husseini AE, Schnell E, Chetkovich DM, Nicoll RA, Brecht DS (2000) PSD-95 involvement in maturation of excitatory synapses. *Science* 290(5495):1364–1368.
79. DeGiorgis JA, Galbraith JA, Dosemeci A, Chen X, Reese TS (2006) Distribution of the scaffolding proteins PSD-95, PSD-93, and SAP97 in isolated PSDs. *Brain Cell Biol* 35(4-6):239–250.
80. Bembem MA, Shipman SL, Nicoll RA, Roche KW (2015) The cellular and molecular landscape of neurologins. *Trends Neurosci* 38(8):496–505.
81. High B, Cole AA, Chen X, Reese TS (2015) Electron microscopic tomography reveals discrete transfect elements at excitatory and inhibitory synapses. *Front Synaptic Neurosci* 7:9.
82. Kerr JM, Blanpied TA (2012) Subsynaptic AMPA receptor distribution is acutely regulated by actin-driven reorganization of the postsynaptic density. *J Neurosci* 32(2):658–673.
83. Shi Y, Lu W, Milstien AD, Nicoll RA (2009) The stoichiometry of AMPA receptors and TARPs varies by neuronal cell type. *Neuron* 62(5):633–640.
84. Mayer ML, Vyklícky L, Jr, Westbrook GL (1989) Modulation of excitatory amino acid receptors by group IIB metal cations in cultured mouse hippocampal neurones. *J Physiol* 415:329–350.
85. Kremer JR, Mastroratte DN, McIntosh JR (1996) Computer visualization of three-dimensional image data using IMOD. *J Struct Biol* 116(1):71–76.
86. Harlow ML, Ress D, Stoschek A, Marshall RM, McMahan UJ (2001) The architecture of active zone material at the frog's neuromuscular junction. *Nature* 409(6819):479–484.